ARTICLES
https://doi.org/10.1038/s41561-018-0085-9
nature geoscience

Observationally derived rise in methane surface forcing mediated by water vapour trends

D. R. Feldman[1,9*], W. D. Collins[1,2,9], S. C. Biraud[1], M. D. Risser[1], D. D. Turner[3], P. J. Gero[4], J. Tadić[1], D. Helmig[5], S. Xie[6], E. J. Mlawer[7], T. R Shippert[8] and M. S. Torn[1,2]

Atmospheric methane (CH_4) mixing ratios exhibited a plateau between 1995 and 2006 and have subsequently been increasing. While there are a number of competing explanations for the temporal evolution of this greenhouse gas, these prominent features in the temporal trajectory of atmospheric CH_4 are expected to perturb the surface energy balance through radiative forcing, largely due to the infrared radiative absorption features of CH_4. However, to date this has been determined strictly through radiative transfer calculations. Here, we present a quantified observation of the time series of clear-sky radiative forcing by CH_4 at the surface from 2002 to 2012 at a single site derived from spectroscopic measurements along with line-by-line calculations using ancillary data. There was no significant trend in CH_4 forcing between 2002 and 2006, but since then, the trend in forcing was 0.026 ± 0.006 (99.7% CI) W m^2 yr^{-1}. The seasonal-cycle amplitude and secular trends in observed forcing are influenced by a corresponding seasonal cycle and trend in atmospheric CH_4. However, we find that we must account for the overlapping absorption effects of atmospheric water vapour (H_2O) and CH_4 to explain the observations fully. Thus, the determination of CH_4 radiative forcing requires accurate observations of both the spatiotemporal distribution of CH_4 and the vertically resolved trends in H_2O.

The globally averaged atmospheric mixing ratio of CH_4 has risen since the pre-industrial epoch from 722 ± 25 ppbv in 1750 to 1803 ± 2 ppbv in 2011[1]. However, there is an unresolved debate regarding the causes of the temporal trajectory of CH_4, and thus its sources and sinks, over the last 30 years. The observed plateau in the CH_4 mixing ratio[2] and its end[3] have been attributed to some combination of changes in hydroxyl (OH) radical destruction, tropical wetland emissions, thawing permafrost and CH_4 hydrates, agriculture, and fossil-fuel extraction and use, although their relative contributions are ambiguous given existing observations[4–10].

Rising atmospheric CH_4 mixing ratios are expected to change the distribution of atmospheric radiative energy, and this is the essential justification for coordinated and prioritized scientific inquiry regarding atmospheric CH_4. While substantial resources have been devoted to measuring increasing atmospheric CH_4 (refs [2,11]) and understanding its anthropogenic contributions[12–14], the observational determination of its radiative forcing has, to date, been limited. Satellite observations have inferred, but not quantified, the radiative forcing associated with rising mixing ratios of this gas[15,16]. Apart from those efforts, radiative forcing values have been strictly calculated by radiative transfer models based on information gathered from laboratory observations. The calculations performed for the IPCC Fifth Assessment Report found that CH_4 has contributed to a stratospherically adjusted long-wave (5–20 μm) radiative forcing at the tropopause of 0.48 ± 0.05 W m^{-2} from the pre-industrial epoch[1]. However, the methods used by that report were last revised in 1998[17], and recent work has indicated that an upward revision to the methane radiative forcing formulae and the determination of its global warming potential for future assessment reports is necessary[18], mostly due to the need to include short-wave effects.

The spectroscopy of CH_4, which is the foundation underlying the radiative forcing calculations, is an active area of research[19]. This is because CH_4 exhibits a line structure of exceptional complexity compared to other atmospheric greenhouse gases[20], and line-by-line calculations and climate model radiation codes must capture this complexity to determine CH_4 radiative forcing. They do so by using line parameters in spectroscopic databases such as High Resolution Transmission (HITRAN)[21] and parameterizations of other absorption effects. These databases are frequently updated, and while the updates have produced only modest changes in CH_4 infrared forcing[22,23], the scientific understanding of other potentially significant absorption effects such as broadening dependencies[24] and H_2O continuum absorption[18,25] is still advancing. Alternatively, we can use field observations to establish the sufficiency of the approach by which CH_4 radiative forcing is solely determined from radiative transfer calculations.

The specialized, long-duration suite of observations collected at the US Department of Energy Atmospheric Radiation Measurement (ARM) Program[26] at the Southern Great Plains (SGP) site (36° 36′ 18″ N, 97° 29′ 6″ W) provide a unique opportunity to observe greenhouse gases and their forcing, as indicated by the first observation of the increase in the greenhouse effect from rising atmospheric concentrations of CO_2 (ref. [27]).

The time series of weekly CH_4 surface flask measurements from SGP shows a high variability in CH_4 at SGP, with boundary-layer excursions sometimes exceeding 2,300 ppbv (Fig. 1). As with other locations of high-precision atmospheric CH_4 measurements, the time series of CH_4 mixing ratios shows fine-scale temporal variability. At SGP, some of the excursions may be due to local hydrocarbon recovery, based on the correlation between CH_4 and ethane mixing

[1]Lawrence Berkeley National Laboratory, Berkeley, CA, USA. [2]University of California-Berkeley, Berkeley, CA, USA. [3]National Oceanic and Atmospheric Administration Earth Systems Research Laboratory, Boulder, CO, USA. [4]University of Wisconsin-Madison, Madison, WI, USA. [5]Institute of Arctic and Alpine Research, University of Colorado-Boulder, Boulder, CO, USA. [6]Lawrence Livermore National Laboratory, Livermore, CA, USA. [7]Atmospheric and Environmental Research, Lexington, MA, USA. [8]Pacific Northwest National Laboratory, Richland, WA, USA. [9]These authors contributed equally: D. R. Feldman and W. D. Collins. *e-mail: drfeldman@lbl.gov

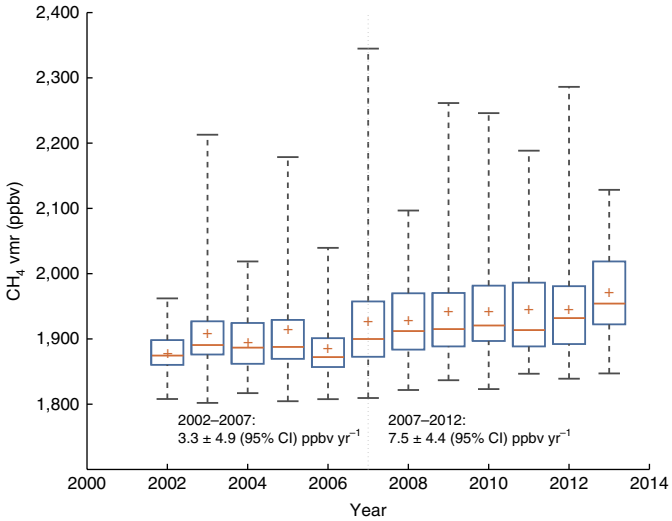

Fig. 1 | Recent evolution of atmospheric methane at the surface study site. Time series of the annual distribution of surface flask measurements of CH_4 volume mixing ratio (vmr) at the DOE ARM SGP site. The box–whisker plots show the mean (+) and median (line), with the box bounding the 25th and 75th percentiles and the whiskers set at the 0.1th and 99.9th percentiles for weekly flask measurements from a given year. Least-squares linear trend analyses are included for selected time periods before and after 2007 (vertical dashed line). The 2007 change point was determined from weekly time-series data (see Methods).

ratios[28,29] (see Methods). Meanwhile, an analysis of these instantaneous CH_4 observations (see Methods) shows no significant trend in atmospheric CH_4 before 2007, a break-point in 2007, and that CH_4 mixing ratios have been rising at a rate of 7.5 ± 4.4 (95% confidence interval (CI)) ppbv yr^{-1} since then.

While other studies have observed trends in the surface energy balance with broadband radiometry[30,31], broadband observations are inadequate for attributing changes in that balance to changes in the atmospheric composition of specific gas species. Therefore, we use a long time series of clear-sky downwelling spectral infrared radiance observations to determine whether changes in atmospheric CH_4 mixing ratios have a discernible effect on the surface energy balance. We focus here on long-wave clear-sky flux changes since they are predicted to be the most sensitive long-wave radiative flux signal associated with rising greenhouse gases[32] and since detailed all-sky forcing calculations of the study site indicate that most of the forcing arises under clear-sky conditions (see Methods).

CH_4 radiative forcing dependencies

Figure 2a shows, through radiative transfer calculations, that the infrared emission by CH_4 that contributes to its long-wave surface radiative forcing occurs predominantly between 1,200 and 1,350 cm^{-1}. However, as the radiative transfer calculations in Fig. 2b show, the determination of CH_4 forcing is complicated by a significant H_2O and N_2O dependence of the downwelling flux in the CH_4 absorption band, arising from the overlap of spectral absorption features of H_2O and N_2O with those of CH_4. The downwelling flux is also highly temperature-dependent, both due to Planck function and absorption line temperature dependence. Fortunately, the surface mixing ratios for N_2O are highly correlated with its mixing ratios throughout the column (Fig. 2c), so the radiative effects of N_2O can be estimated using a near-surface measurement of its mixing ratio. Radiosonde data at the ARM SGP site were used to control for variability in the atmospheric thermodynamic state[33]. Airborne measurements indicate that boundary-layer and free tropospheric fluctuations in CH_4 mixing ratios are not highly correlated at subseasonal timescales. Therefore, surface observations of CH_4 mixing ratio alone are insufficient for calculating CH_4 forcing at the timescales of our analysis.

CH_4 surface radiative forcing was derived from 11 years of infrared spectroscopic observations made by the Atmospheric Emitted Radiance Interferometer (AERI)[34]. The forcing was determined by differencing AERI measurements with counterfactual line-by-line calculations[27] where the thermodynamic state is prescribed by concurrent radiosonde observations[33], but the calculation used a pre-industrial CH_4 mixing ratio (see Methods). Detailed data quality control and averaging methods were used to account for the effects of uncertainties in temperature, H_2O and N_2O, and the effect of instrumental noise, respectively (see Methods). The minimum temporal resolution of the observations used here was 6 h (see Methods). From this process chain, we observe the direct, unadjusted, instantaneous radiative forcing at the surface, which, while not biased by the effects of thermodynamics (see Methods), is still affected by them. Ideally, measurements would be made under prescribed thermodynamic conditions, but we have no means of controlling for these conditions in the field.

The mean spectral residuals were prominent only in the spectral region of CH_4 absorption (see Methods) and therefore exclude the possibility that uncertainties in the atmospheric state and instrument calibration were substantially affecting the results. Top-down validation of our forcing estimates, based on in situ observations by simultaneous aircraft overflights[35], indicates that we can observe instantaneous CH_4 forcing to within 0.14 W m^{-2} (see Methods). Sensitivity tests (see Methods) reveal that the transient plumes of boundary-layer methane would lead to an instantaneous surface radiative forcing signal of 0.05 W m^{-2}, so our analysis is unable to discern the transient contribution of anthropogenic activity to observed forcing. However, supraseasonal time-series features of atmospheric CH_4 mixing ratios, which do contain contributions from human activity[4–10], are readily discernible in the observed radiative forcing.

Observation-derived forcing and thermodynamic influences

Irrespective of the source of the atmospheric CH_4, we derive a time series of CH_4 surface long-wave radiative forcing from observations that exhibits several prominent features (Fig. 3). During the multi-year atmospheric CH_4 plateau, the trend in this forcing did not differ significantly from zero ($P > 0.1$). The time series exhibited a significant change around 2007 at the end of the plateau ($P < 0.0001$). From then onwards, the trend differed from zero at 0.026 ± 0.006 W m^{-2} yr^{-1} (99.7% CI). During the 11-year record, there was a large seasonal cycle, with an amplitude of at least 0.2 W m^{-2}.

During the time period of the atmospheric CH_4 plateau, it is expected that there would not be significant trends in surface radiative forcing from CH_4, and this was confirmed by observations. However, the amplitude of the seasonal cycle in surface forcing throughout the time series and the forcing trend since 2006 cannot be fully explained by the atmospheric CH_4 mixing ratio at the SGP. The amplitude of the seasonal cycle in a CH_4 dry atmospheric mixing ratio is 51.2 ± 10.1 (99.7% CI) ppbv, and, based on the mean water vapour profile during the observational period at the SGP, the seasonal cycle amplitude would be 0.012 ± 0.002 (99.7% CI) W m^{-2}, significantly smaller than the observed amplitude of 0.25 ± 0.01 (99.7% CI) W m^{-2}. The observed trend in CH_4 since 2007 is 7.5 ± 6.6 (99.7% CI) ppbv yr^{-1}, which, again based on the mean water vapour profile during the observational period at the SGP, would yield a trend of 0.002 ± 0.0009 (99.7% CI) W m^{-2} yr^{-1}, significantly smaller than the observed trend of 0.026 ± 0.006 (99.7% CI) W m^{-2} yr^{-1}. However, analysing the time series in isolation from thermodynamics is highly idealized, can yield varying

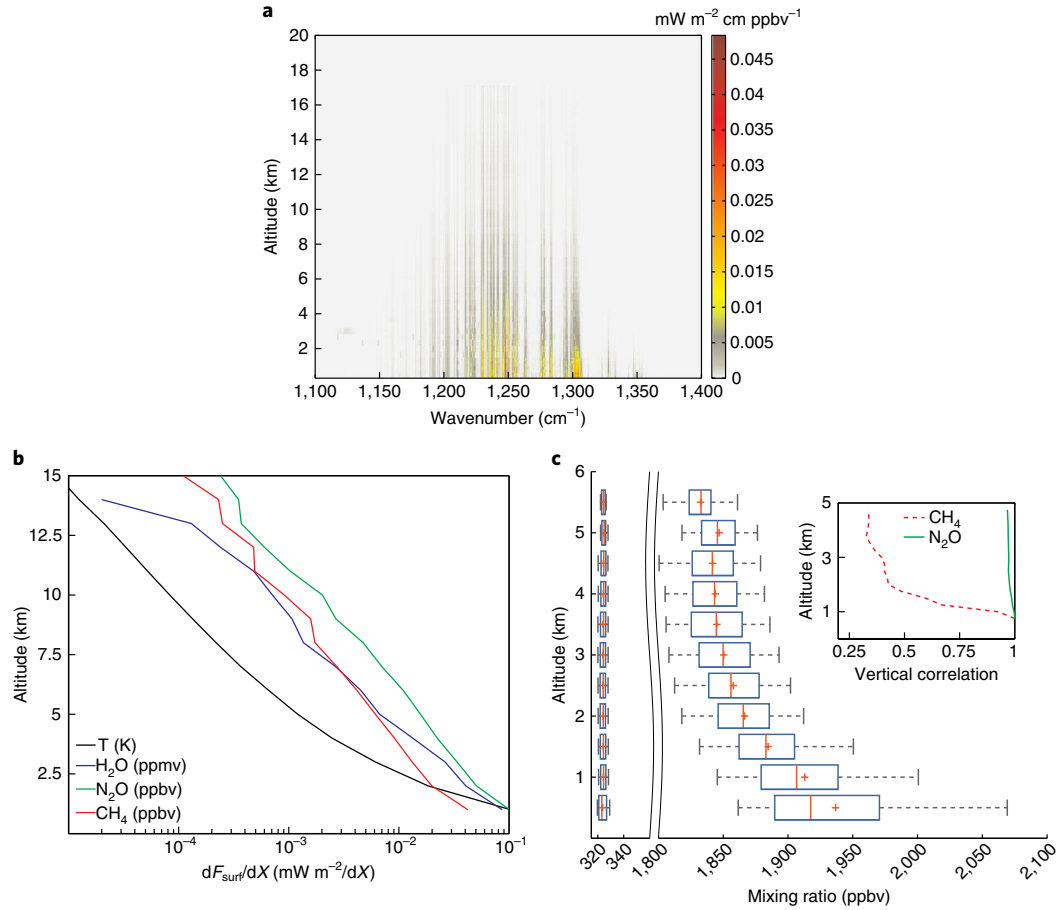

Fig. 2 | Factors affecting CH_4 long-wave surface instantaneous radiative forcing. a, Change in spectral flux for a 1 ppbv perturbation in CH_4 for a 1 km layer in a mid-latitude summer profile[44]. **b**, Vertical sensitivity of the downwelling surface flux in the CH_4 absorption band (1,200 and 1,350 cm^{-1}) to 1 km perturbations in temperature, H_2O, N_2O and CH_4 derived from Line-by-Line Radiative Transfer Model (LBLRTM) calculations with the mid-latitude summer profile. **c**, Box-whisker diagrams of the vertical distribution of CH_4 and N_2O, with the inset showing the associated correlation coefficient in the mixing ratio between the surface and a given height, from aircraft observations[35] at SGP from flights in 2002–2012. The box spans the 25th to 75th percentile, and the whiskers span the 5th to 95th percentile of the observations.

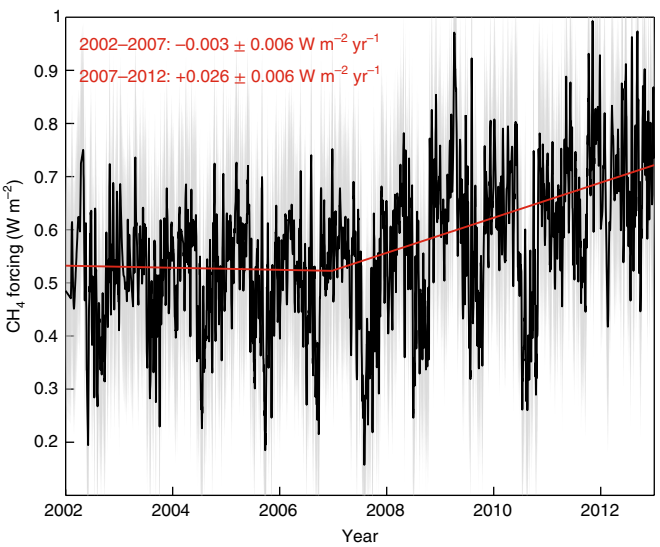

Fig. 3 | CH_4 long-wave surface radiative forcing time series at SGP. Time series (black), 2σ instantaneous uncertainty in CH_4 surface long-wave radiative forcing (grey; see Methods) and trends with 3σ uncertainty (red; see Methods.) at DOE ARM SGP.

results depending on the choice of thermodynamic conditions, and is inconsistent with actual conditions in the field. Nevertheless, this discrepancy must be resolved.

We can exclude several potential explanations for these findings; for example, the contributions of observational error and analysis error would produce spectral residuals outside the CH_4 absorption band and time-series statistics that are inconsistent with our findings. Possible contributions from other radiatively active trace gases in the CH_4 absorption band between 1,200 and 1,350 cm^{-1} can also be excluded (see Methods).

Rather, we find that when we perform a multivariate signal decomposition analysis of the deseasonalized time series of CH_4 forcing constructed over the entire time series using a nonlinear predictor based solely on CH_4 concentrations, we can explain roughly 80% of the variation in observed forcing ($R^2 = 0.793$), implying that at least 20.7% of the variance is related to other factors (see Methods).

Here, we find that the contribution of trends and variability in water vapour to those in CH_4 surface forcing are significant. Even though the residual spectra indicate that we are not imprecisely specifying atmospheric temperature and moisture, CH_4 forcing is nonetheless dependent on atmospheric state. The primary reason for this water vapour dependence is that mid-infrared CH_4 absorption occurs at the edge of a strong ν_2 H_2O absorption band. Therefore,

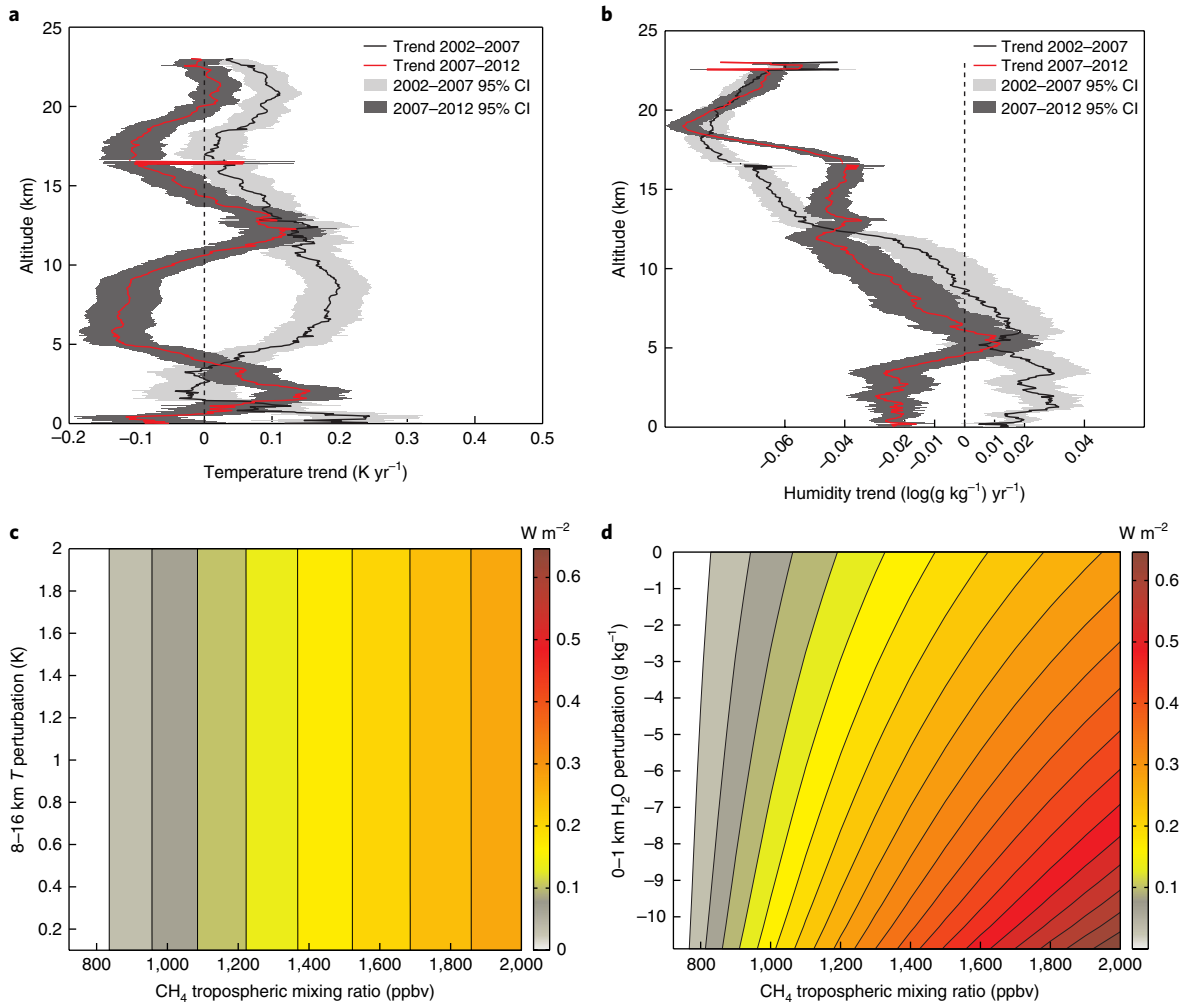

Fig. 4 | Thermodynamic dependence of CH_4 surface forcing. a, Vertically resolved trends in ARM Best Estimate temperature measurements with the 99.7% CI. **b**, The same as **a**, but for trends in the logarithm of specific humidity. **c**, Surface radiative forcing versus tropospheric-averaged CH_4 as a function of temperature perturbations from 8 to 16.5 km from a mid-latitude summer atmosphere[44]. The change in mid-level temperature over the observed time period was 0.4 ± 0.2 K (99.7% CI) and is indicated on the plot. **d**, The same as **c**, but for humidity perturbations in grams per kilogram from 0 to 1 km. The change in boundary-layer water vapour over the observed time period was -1.5 ± 1.0 g kg^{-1} (99.7% CI) and is indicated on the plot.

elevated H_2O mixing ratios saturate the CH_4 band[36] and reduce the latter molecule's radiative forcing, as shown in Fig. 4d. Indeed, we performed a model-only computation based on observed thermodynamics and CH_4 mixing ratios and obtain a trend of 0.020 ± 0.009 (99.7% CI) W m^{-2} yr^{-1}, which is not distinguishable ($P > 0.05$) from the observationally derived trend. In addition, this effect is largely insensitive to the observed mid-tropospheric temperature changes, as shown in Fig. 4c.

For the seasonal cycle, we find that the water vapour seasonal cycle of 7.7 ± 0.03 g kg^{-1} helps explain the seasonal cycle in observed CH_4 surface forcing. For trends, we note that a long-term decreasing trend in moisture availability in the central United States has been observed[37]. This was also observed in a 14-year analysis of AERI clear-sky radiances[38]. At the SGP, an analysis of radiosondes coincidental to the CH_4 forcing observations is consistent with that finding and yields negative trends in atmospheric moisture in the lowest 1 km, as shown in Fig. 4b. While no significant change point in the vertically resolved time series is observed, column water decreased by 30% since the end of the CH_4 plateau. This negative trend over the entire time series and especially since the end of the CH_4 plateau will tend to enhance CH_4 forcing, and provides the opportunity to analyse the alternating effects of CH_4 and H_2O on the observed forcing. Figure 5 shows that the observed forcing trends in CH_4 forcing could be reproduced only when we include nonlinear predictors that include both CH_4 concentration and observed thermodynamic trends ($R^2 = 0.997$, see Methods). Specifically, trends in CH_4 surface flask measurements and trends in height-resolved temporal profiles of temperature and humidity can be used to predict both plateau and post-plateau surface radiative forcing trends after all variables are decomposed into frequency noise (Fig. 5a), a seasonal component (Fig. 5b) and deseasonalized trends (Fig. 5c), yielding a normally distributed residual signal (Fig. 5d). The result is that the first temperature and moisture principal components, covering the lower 5 km of the atmosphere, explain nearly all of the signal's variance (Fig. 5e,f).

Broader implications

This study presents the first observational derivation and quantification of the effect of time-varying CH_4 on the clear-sky surface energy balance, with a large seasonal cycle amplitude of 0.25 W m^{-2} and a significant difference in forcing trends at the SGP during and after the CH_4 plateau. The decadally averaged trend in surface forcing was larger for CO_2 than CH_4 at this site, but the perturbation of the surface energy balance from rising CH_4 mixing ratios since

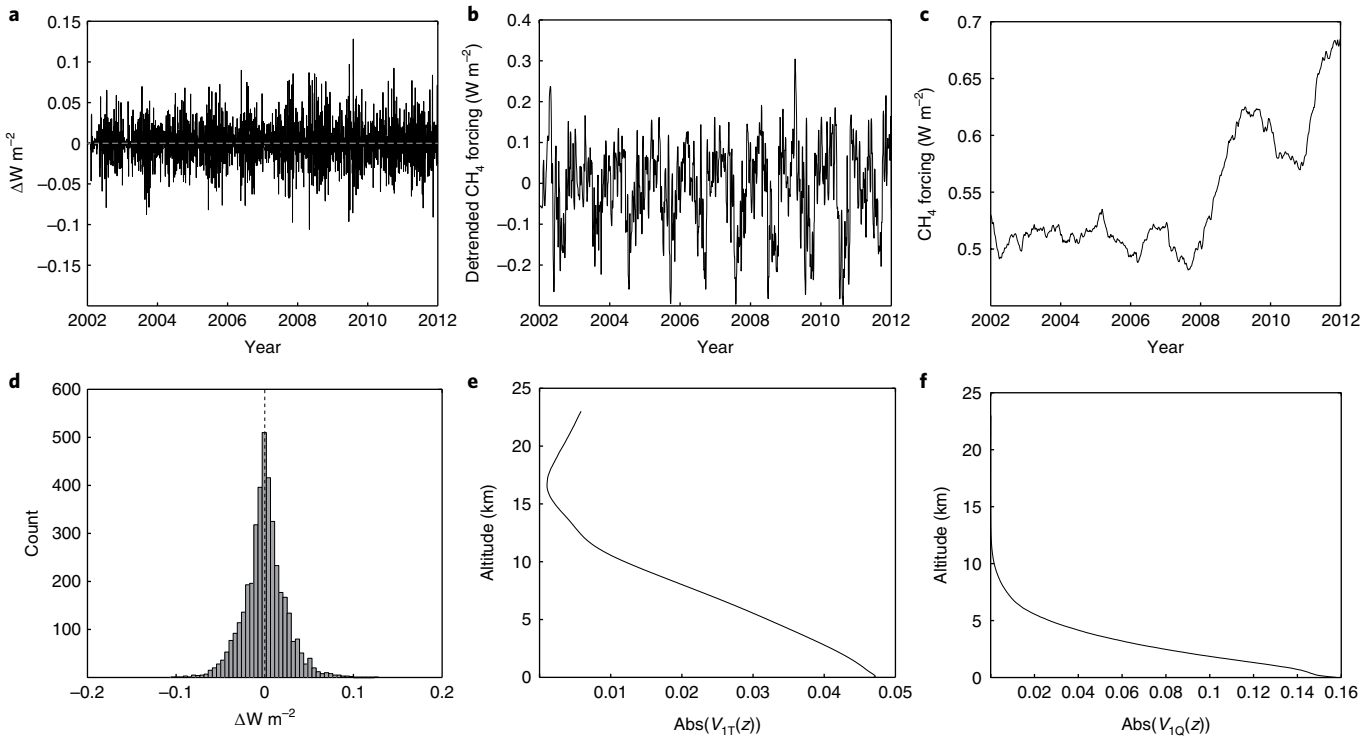

Fig. 5 | Forcing time-series decomposition and reconstruction from predictors. a, Time series of CH_4 forcing signal noise removed by a random forest with 100 weak learners. **b**, Seasonal component of the CH_4 forcing signal. **c**, Deseasonalized CH_4 forcing signal. **d**, Histogram of observed versus decomposed and reconstructed forcing. **e**, First component of principal component analysis of temperature predictors. **f**, First component of principal component analysis for humidity predictors. See Methods for details.

the end of the plateau was similar to the effect from rising CO_2 ($0.02 \pm 0.007\,W\,m^{-2}\,yr^{-1}$) at the site. Although this difference was not statistically significant ($P > 0.3$), it suggests that, since the end of the plateau, the role of rising CH_4 in perturbing the surface energy balance can be highly dependent on local water vapour trends[39–42]. At the SGP, CH_4 surface forcing trends are not necessarily inferior to that of CO_2, even though forcing at the tropopause by CO_2 is much more than that from CH_4 (ref. [1]).

These observations show a long-term trend in CH_4 surface radiative forcing, with variance from a function of rising CH_4 mixing ratios and the non-negligible contribution that depends on the vertical distribution of water vapour. This finding is related to tropopausal radiative forcing, which figures prominently in the scientific discussion of how rising CH_4 impacts average tropospheric temperatures[1], but spatial patterns in upper tropospheric moisture[43] mediate forcing at the tropopause, while surface humidity more strongly affects surface forcing. For this investigation, we find that trends in surface forcing from greenhouse gases are convolved with the details of how the thermodynamic state of the atmosphere is evolving, and the local thermodynamic conditions must be taken into account. Since local temperature and humidity trends that are distinct from those at the SGP exist at other sites, the relative contributions of thermodynamics and mixing ratio changes to the forcing may also differ. Observed trends in surface humidity have not been spatially or temporally uniform, nor have they been monotonic. The magnitude of the globally averaged land-surface humidity trend varies on decadal timescales while also exhibiting trends that are spatially variable over land and that show strong land–ocean contrast[39–42]. Therefore, the direct impact of greenhouse gases on the surface energy balance cannot be predicted in isolation from thermodynamics. Nevertheless, as we have shown, CH_4 surface radiative forcing trends can be derived from measurements and quantified spectroscopically.

Methods

Methods, including statements of data availability and any associated accession codes and references, are available at https://doi.org/10.1038/s41561-018-0085-9.

Received: 1 June 2017; Accepted: 22 February 2018;
Published online: 2 April 2018

References

1. Myhre, G. et al. in *Climate Change 2013: The Physical Science Basis* (eds Stocker, T. F. et al.) Ch. 8 (IPCC, Cambridge Univ. Press, Cambridge, 2013).
2. Dlugokencky, E. J., Nisbet, E. G., Fisher, R. & Lowry, D. Global atmospheric methane: budget, changes and dangers. *Phil. Trans. R. Soc. Lond. Ser. A* **369**, 2058–2072 (2011).
3. Nisbet, E. G., Dlugokencky, E. J. & Bousquet, P. Methane on the rise—again. *Science* **343**, 493–495 (2014).
4. Kirschke, S. et al. Three decades of global methane sources and sinks. *Nat. Geosci.* **6**, 813–823 (2013).
5. Aydin, M. et al. Recent decreases in fossil-fuel emissions of ethane and methane derived from firn air. *Nature* **476**, 198–201 (2011).
6. Kai, F. M., Tyler, S. C., Randerson, J. T. & Blake, D. R. Reduced methane growth rate explained by decreased Northern Hemisphere microbial sources. *Nature* **476**, 194–197 (2011).
7. Schaefer, H. et al. A 21st century shift from fossil-fuel to biogenic methane emissions indicated by $^{13}CH_4$. *Science* **352**, 80–84 (2016).
8. Prather, M. J. & Holmes, C. D. Overexplaining or underexplaining methane's role in climate change. *Proc. Natl Acad. Sci. USA* **114**, 5324–5326 (2017).
9. Rigby, M. et al. Role of atmospheric oxidation in recent methane growth. *Proc. Natl Acad. Sci. USA* **114**, 5373–5377 (2017).
10. Turner, A. J., Frankenberg, C., Wennberg, P. O. & Jacob, D. J. Ambiguity in the causes for decadal trends in atmospheric methane and hydroxyl. *Proc. Natl Acad. Sci. USA* **114**, 5367–5372 (2017).
11. Bergamaschi, P. et al. Atmospheric CH_4 in the first decade of the 21st century: inverse modeling analysis using SCIAMACHY satellite retrievals and NOAA surface measurements. *J. Geophys. Res.* **118**, 7350–7369 (2013).
12. Turner, A. J. et al. A large increase in U.S. methane emissions over the past decade inferred from satellite data and surface observations. *Geophys. Res. Lett.* **43**, 2218–2224 (2016).

13. Miller, S. M. et al. Anthropogenic emissions of methane in the United States. *Proc. Natl Acad. Sci. USA* **110**, 20018–20022 (2013).
14. Brandt, A. R. et al. Methane leaks from North American natural gas systems. *Science* **343**, 733–735 (2014).
15. Harries, J. E., Brindley, H. E., Sagoo, P. J. & Bantges, R. J. Increases in greenhouse gas forcing inferred from outgoing longwave spectra of the Earth in 1970 and 1997. *Nature* **410**, 355–357 (2001).
16. Griggs, J. A. & Harries, J. E. Comparison of spectrally resolved outgoing longwave radiation over the tropical Pacific between 1970 and 2003 using IRIS, IMG, and AIRS. *J. Clim.* **20**, 3982–4001 (2007).
17. Myhre, G., Highwood, E. J., Shine, K. P. & Stordal, F. New estimates of radiative forcing due to well mixed greenhouse gases. *Geophys. Res. Lett.* **25**, 2715–2718 (1998).
18. Etminan, M., Myhre, G., Highwood, E. J. & Shine, K. P. Radiative forcing of carbon dioxide, methane, and nitrous oxide: a significant revision of the methane radiative forcing. *Geophys. Res. Lett.* **43**, 12614–12623 (2016).
19. Brown, L. R. et al. Methane line parameters in the HITRAN2012 database. *J. Quant. Spectrosc. Rad. Trans.* **130**, 201–219 (2013).
20. Goody, R. M. & Yung, Y. L. (eds) in *Atmospheric Radiation: Theoretical Basis* Ch. 3 (Oxford Univ. Press, New York, 1989).
21. Rothman, L. S. et al. The HITRAN2012 molecular spectroscopic database. *J. Quant. Spectrosc. Rad. Trans.* **130**, 4–50 (2013).
22. Kratz, D. P. The sensitivity of radiative transfer calculations to the changes in the HITRAN database from 1982 to 2004. *J. Quant. Spectrosc. Rad. Trans.* **109**, 1060–1080 (2008).
23. Lu, P., Zhang, H. & Jing, X. The effects of different HITRAN versions on calculated long-wave radiation and uncertainty evaluation. *Acta Meteor. Sin.* **26**, 389–398 (2012).
24. Delahaye, T. et al. Measurements of H_2O broadening coefficients of infrared methane lines. *J. Quant. Spectrosc. Rad. Trans.* **173**, 40–48 (2016).
25. Mlawer, E. J. et al. Development and recent evaluation of the MT_CKD model of continuum absorption. *Phil. Trans. R. Soc. A* **370**, 2520–2556 (2012).
26. Turner, D. D. & Ellingson, R. G. *The Atmospheric Radiation Measurement Program: The First 20 Years* (Amer. Meteor. Soc., Boston, 2016).
27. Feldman, D. R. et al. Observational determination of surface radiative forcing by CO_2 from 2000 to 2010. *Nature* **519**, 339–343 (2015).
28. Helmig, D. et al. Reversal of global atmospheric ethane and propane trends largely due to US oil and natural gas production. *Nat. Geosci.* **9**, 490–495 (2016).
29. Hausmann, P., Sussmann, R. & Smale, D. Contribution of oil and natural gas production to renewed increase in atmospheric methane (2007–2014): top-down estimate from ethane and methane column observations. *Atmos. Chem. Phys.* **16**, 3227–3244 (2016).
30. Wild, M. et al. The global energy balance from a surface perspective. *Clim. Dynam.* **40**, 3107–3134 (2013).
31. Wang, K. & Liang, S. Global atmospheric downward longwave radiation over land surface under all-sky conditions from 1973 to 2008. *J. Geophys. Res.* **114**, D19101 (2009).
32. Stephens, G. L. et al. An update on Earth's energy balance in light of the latest global observations. *Nat. Geosci.* **5**, 691–696 (2012).
33. Xie, S. et al. Clouds and more: ARM climate modeling best estimate data. *Bull. Am. Meteor. Soc.* **91**, 31–20 (2010).
34. Knuteson, R. O. et al. Atmospheric emitted radiance interferometer. Part I: Instrument design. *J. Atmos. Ocean. Technol.* **21**, 1763–1776 (2004).
35. Biraud, S. C. et al. A multi-year record of airborne CO_2 observations in the US Southern Great Plains. *Atmos. Meas. Tech.* **6**, 751–763 (2013).
36. Huang, Y., Tan, X. & Xia, Y. Inhomogeneous radiative forcing of homogeneous greenhouse gases. *J. Geophys. Res.* **121**, 2780–2789 (2016).
37. Jung, M. et al. Recent decline in the global land evapotranspiration trend due to limited moisture supply. *Nature* **467**, 951–954 (2010).
38. Gero, P. J. & Turner, D. D. Long-term trends in downwelling spectral infrared radiance over the U.S. Southern Great Plains. *J. Clim.* **24**, 4831–4843 (2011).
39. Willett, K. M. et al. HadISDH: an updateable land surface specific humidity product for climate monitoring. *Clim. Past* **9**, 657–677 (2013).
40. Dai, A. Recent climatology, variability, and trends in global surface humidity. *J. Clim.* **19**, 3589–3606 (2006).
41. Berry, D. I. & Kent, E. C. A new air-sea interaction gridded dataset from ICOADS with uncertainty estimates. *Bull. Am. Meteor. Soc.* **90**, 645–656 (2009).
42. Simmons, A. J., Willett, K. M., Jones, P. D., Thorne, P. W. & Dee, D. P. Low frequency variations in surface atmospheric humidity, temperature, and precipitation: inferences from reanalyses and monthly gridded observational data sets. *J. Geophys. Res.* **115**, D01110 (2010).
43. Wentz, F. J., Ricciardulli, L., Hilburn, K. & Mears, C. How much more rain will global warming bring? *Science* **317**, 233–235 (2007).
44. Anderson, G. P. et al. *AFGL Atmospheric Constituent Profiles (0–120 km)* AFGL-TR_86-0110 (AFGL, 1989).

Acknowledgements

This material is based on work supported by the Director, Office of Science, Office of Biological and Environmental Research of the US Department of Energy (DOE) under contract no. DE-AC02-05CH11231 as part of their Atmospheric System Research (ASR) Program, the Atmospheric Radiation Measurement (ARM) Program, the Terrestrial Ecosystem Sciences (TES) Programs, and the ARM Aerial Facility (AAF). Resources of the National Energy Research Scientific Computing Center (NERSC) were used under the same contract. Work at LLNL was performed under the auspices of the US DOE by Lawrence Livermore National Laboratory under contract no. DE-AC52-07NA27344. M. Alvarado, K. Cady-Pereira, L. Riihimaki, I. Simpson and P. Novelli also contributed. NOAA GMD provided flask CH_4, C_2H_6 and N_2O data.

Author contributions

D.R.F. led the research, performed all calculations and wrote the manuscript; W.D.C. proposed the study concept, provided research guidance and conceived methods for isolating the CH_4 signal; S.C.B. provided CH_4 and N_2O data and associated support; M.D.R. provided the statistical analysis; D.D.T. provided guidance on AERI instrument performance and research focus; P.J.G. helped interpret AERI data; J.T. analysed thermodynamic contributions to the observed forcing. D.H. provided C_2H_6 data and associated support; S.X. provided ARMBE data and associated support; E.J.M. and T.R.S. provided clear-sky error analysis; M.S.T. provided research feedback and guidance and served as the principal investigator of the grant supporting this research. All authors discussed the results and commented on the manuscript.

Competing interests

The authors declare no competing interests.

Additional information

Supplementary information is available for this paper at https://doi.org/10.1038/s41561-018-0085-9.

Reprints and permissions information is available at www.nature.com/reprints.

Correspondence and requests for materials should be addressed to D.R.F.

Publisher's note: Springer Nature remains neutral with regard to jurisdictional claims in published maps and institutional affiliations.

Methods

CH_4 surface radiative forcing was determined by differencing measured spectra from the AERI instrument[45], subject to quality control (see below), with radiative transfer calculations using 512 levels of temperature and humidity from radiosondes profiles as processed by the ARM Best Estimates (ARMBEs)[33,46], ozone from the Modern-Era Retrospective Analysis for Research and Applications (MERRA)[47], CO_2 profiles from the nearest spatiotemporal grid point from CarbonTracker-CO2 2013[48], monthly averaged N_2O mixing ratios from the Mauna Loa Observatory (MLO)[49] and pre-industrial (722 ppbv) CH_4 mixing ratios. This counterfactual calculation, designed to simulate the spectrally resolved radiance field at the Earth's surface, had CH_4 mixing ratios that remained at annually averaged pre-industrial levels[27]. The counterfactual was created with the Line-by-Line Radiative Transfer Model (LBLRTM) version 12.2, using the Atmospheric and Environmental Research (AER) line parameter database version 3.1[50] based on HITRAN 2008[51] with updated line-mixing[52] and the MT_CKD_2.5.2 H_2O continuum absorption model[25]. Limb-brightening factors, converting both observations and calculations from radiance to flux, were calculated with three-point Gaussian quadrature over the zenith angle[53]. Supplementary Fig. 1 shows a schematic of this process chain.

Data quality control. AERI spectra were recorded every 8 min from the instrument's initial deployment to April 2004 (at the SGP). Subsequently, spectra were recorded every 30 s, with only minor outages, to provide higher-temporal-resolution data for cloud studies[54]. This analysis considered only data starting in 2002 because the ARMBE data are derived from Vaisala RS-80 profiles before 2002 and that instrument suffered a known dry bias[55,56]. The end of the analysis period was the start of 2013, which was chosen because the AERI instrument at SGP experienced a failure and was replaced in mid-2013. The analysis could be extended beyond early 2013, but would have to address complications from changing instrumentation[57].

Only the subset of spectra recorded within 2 h of a radiosonde launch were utilized. With 4 daily launches, each measurement is separated by a minimum of 6 h and spans 4 h. Based on the radiosonde profile, a radiance spectrum was calculated using LBLRTM with 512 levels of temperature and relative humidity from the ARMBE product[33]. All AERI spectra recorded within 2 h of the radiosonde launch were rank-ordered by the root-mean-squared brightness temperature of the residual spectrum of the difference between the measurement and the LBLRTM calculation between 600 and 980 cm^{-1}. This range was chosen to be sensitive to thermodynamic conditions but insensitive to CH_4 or ozone, where the latter is strongly influenced by MERRA biases[58]. The rank-ordered spectra were averaged sequentially together (that is, the first two spectra were averaged, then the first three spectra were averaged and so on) and the r.m.s. of the residual between that average and the LBLRTM calculation was recalculated. The sequential average of the spectra that produced the minimum r.m.s. of the residual relative to the radiosonde-based LBLRTM calculation was used as the AERI spectral measurement for subsequent analysis. The rationale for this approach is to average as many spectra together as possible to minimize random measurement error, but to avoid biasing the spectra by averaging observations during which clouds were present or where the thermodynamic conditions had changed relative to the radiosonde.

Since the determination of CH_4 surface forcing is so dependent on an accurate specification of the atmospheric thermodynamic profile, we apply additional tests of the sequentially averaged spectra against the counterfactual calculations to remove cases where the thermodynamic or condensate profiles differ substantially between the observation and the counterfactual. First, we evaluate the r.m.s. of the residual between the AERI spectral measurement and the LBLRTM calculation between 790 and 810 cm^{-1} (hereafter referred to as the 800 cm^{-1} channel), because this region is sensitive to atmospheric temperature, humidity and condensates (see Supplementary Fig. 2a,b). These plots show the slope and correlation coefficient of the least-squares relationship between the radiative flux sensitivity to moisture and temperature perturbations for a given channel outside the CH_4 absorption feature (1,200–1,350 cm^{-1}) and the average radiative flux sensitivity to moisture and temperature perturbations within the CH_4 absorption feature. The least-squares relationship is derived from six model atmospheres, which span a wide range of terrestrial thermodynamic conditions[44]. The upper panels of Fig. 2a,b show that fluxes in the spectral region between 790 and 810 cm^{-1} are more sensitive to perturbations in temperature and moisture than fluxes in the CH_4 absorption band. The lower panels show that perturbations in temperature and moisture produce flux perturbations in the 790–810 cm^{-1} spectral region and the CH_4 absorption band that are highly correlated.

We also utilize the r.m.s. of the residual between 705 and 709 cm^{-1} (hereafter referred to as the 707 cm^{-1} channel), which is sensitive to the atmospheric boundary-layer temperature. Supplementary Fig. 2c shows the gain and correlation coefficient for the relationship between the variance of a spectral channel outside the CH_4 absorption feature and the variance of the spectral channel within the CH_4 absorption feature, where both are calculated with the measurements and calculations used in the aircraft validation cases (see below). This figure shows that the 707 cm^{-1} variance is highly correlated with the variance within the CH_4 band across a range data wherein the 800 cm^{-1} tolerance criterion is satisfied below 5 K. A gain of greater than unity, indicating high sensitivity to boundary-layer temperature perturbations, is also shown at 707 cm^{-1} for the same 800 cm^{-1} tolerance criterion.

Only spectral residuals with a r.m.s. residual spectrum brightness temperature at 800 cm^{-1} of less than 3 K and a standard deviation at 707 cm^{-1} of less than 0.3 K (after averaging) are considered for subsequent analysis. See Supplementary Information for the rationale for these threshold choices.

Supplementary Fig. 4 shows the average residual spectrum featuring a large deviation from zero where CH_4 has a prominent absorption due to the use of a pre-industrial CH_4 mixing ratio for the counterfactual calculation and deviations equivalent to less than 1 K in temperature, 10 ppmv CO_2, 5% H_2O and 10% N_2O. The exception lies in the 9.6 μm ozone absorption band between 980 and 1080 cm^{-1}, indicating a systematic overestimation of column ozone from the MERRA data products at SGP[58]. The lack of prominent spectral structures outside the CH_4 and O_3 bands excludes other possible explanations including cloud contamination, water vapour or temperature bias or instrument calibration, all of which produce spectral residuals with characteristic features not solely in the CH_4 absorption band.

Time-series decomposition. We tested the hypothesis that the cause for the observed trend in radiative forcing could be contained within a set of predictors including height-resolved trends in water vapour, height-resolved trends in temperature and ground-level methane concentration measured by flasks. If we cannot use these predictors to reproduce the observed forcing, we can infer that there are other contributing factors to the forcing that we have not considered. For the reconstruction of this time series, we used a two-step decomposition of all predictors using a widely utilized and flexible approach that avoids over-fitting[59]. First, we isolated the component of the unfiltered signal that cannot be described as white noise or outlier data using a calibrated random forest with 100 weak learners[59]. A calibrated random forest was used to reproduce the signal at the desired points in time, and the difference between the reproduced and actual signal was filtered out. Second, the remaining noise and cyclical components of the signal were removed using a moving-average filter with a 12-month window[60]. The size of the moving-average filter window was selected because the signal exhibited clear annual seasonal variations.

With this approach, we created a set of isolated trends for 1,025 predictors (512 each for temperature and humidity and 1 for flask CH_4 observations). To make the problem less computationally expensive, and given the extreme level of redundancy in vertically resolved temperature and water-vapour predictors, we applied principal component analysis for the reduction of dimensionality[61]. The fraction of variance explained by the first 5 principal components (out of 512) was found to be > 99.99% for both temperature and humidity, confirming the high degree of redundancy in the predictors. With 5 PCs for temperature, 5 for humidity and 1 for methane concentration, we created a reduced set of 11 predictors to describe the CH_4 radiative forcing trend. An ensemble of five back-propagation neural networks was then trained to reproduce the trend component of the CH_4 radiative forcing[62]. To avoid over-fitting, the training and reproduction of the radiative forcing was done in a leave-one-out fashion, such that the radiative forcing value to be reconstructed from the predictors is withheld from the training set. Instead, ensemble neural networks are trained using the remaining data points, and then the network is used to reproduce the withheld data point. The procedure was repeated sequentially for all data points.

With this approach, the correlation coefficient between the observed trends in the entire CH_4 surface forcing time series and the neural network prediction where all 11 predictors are used is 0.9983 ($R^2 = 0.997$). Where only the CH_4 flask data are used as a predictor to train the network, the correlation coefficient is 0.8907 ($R^2 = 0.793$). More specifically, we can explain ~80% of the variance in radiative forcing using custom-designed nonlinear predictor. However, we should note that our signal is obtained from the difference between an observation and calculation, which is not the best possible nonlinear predictor, so the amount of variance that can be explained using only CH_4 concentrations is necessarily less that 80%. Rather, our results produce an estimate of the minimum of the fraction of variance that cannot be explained using the predictor(s) of interest. They also show that information from temperature and humidity, and not just CH_4 flask concentration data, is needed to describe the observed trend in CH_4 surface radiative forcing.

Statistical analysis methods. The statistical analysis of the time series seeks to determine whether and when a change point occurred in the measured CH_4 surface radiative forcing, as well as the linear (temporal) trends and their significance. The following describes the methods used to perform this analysis.

Define y_t as the CH_4 forcing for the SGP site at time $t = 1,\ldots, T$. Our statistical model is:

$$y_t = b_0 + b_1 t + b_2 X_t (t - t_0) + a_j + e_t + v_t \quad (1)$$

where $\{b_k\}$ are unknown regression coefficients, $\{a_j\}$ represent (unknown) monthly effects, e_t are independent and identically distributed (iid) $N(0, s^2)$ with s^2 unknown ($N(a, b)$ denotes a univariate Gaussian random variable with mean a and variance b), and v_t iid $N(0, w^2)$ with w^2 known (also, e_t and v_t are independent).

The model (1) contains two error processes: first, e_t represents error in the model specification and therefore s^2 is estimated; second, v_t represents error introduced by the measurement process on yt and therefore w^2 will be considered fixed (see the section entitled Statistical analysis results). The variable X_t is defined to be 0 if $t \le t_0$ and 1 if $t > t_0$, and the change point must fall between fixed bounds $T_U < t_0 < T_L$. Therefore, for $t \le t_0$, the monthly adjusted trend in expected CH_4 forcing has slope b_1; for $t > t_0$, the trend has slope $b_1 + b_2$.

The unknown parameters in (1) and the change point can be estimated using a common (frequentist) statistical technique called maximum likelihood[63], which also yields CIs for the regression coefficients[64]. Given the set-up in (1), we can determine the significance of the change point t_0 by way of model selection: the full model (1) can be compared to a 'reduced' model without a change point (H_1: $b_2 \neq 0$):

$$y_t = b_0 + b_1 t + a_j + e_t + v_t \quad (2)$$

A test of H_0 can be performed using a standard full versus reduced model F-test for nested models[64].

The frequentist analysis described above ignores any uncertainty in estimating the change point, and the model is not well suited to assess this uncertainty (outside of asymptotic evaluations)[65]. Alternatively, a Bayesian approach can be used to determine the significance of the change point while accounting for its uncertainty (again using model comparison). Bayesian models that mirror the full (1) and reduced (2) models can be set up using non-informative prior distributions and estimated using Markov chain Monte Carlo methods[66]. Markov chain Monte Carlo output can be used to compare the full and reduced models using Bayes factors[67].

Statistical analysis results. The aforementioned models were fit for many different data sets from the SGP site. This data set was created by using values of the 800 cm^{-1} brightness temperature residual threshold parameter ranging from 0.1 to 10 (see the section entitled Data quality control). However, if the data set for a particular threshold value had fewer than 50 observations, the analysis was not conducted. The lower and upper limits of the change point were fixed to $T_L = 2004$ and $T_U = 2010$; any potential change points near the beginning or end of the time series are not of interest. The seasonal cycle of CH_4 due to hydroxyl radical destruction is captured via the monthly effects $\{a_j\}$; for comparison, all models were fitted and the results are presented both with and without the monthly effects.

For the maximum-likelihood models, plots of the estimated change point, significance of the change point, and estimates of the slope parameters (with 99.7% CIs) from both before and after the change point are provided in Supplementary Figs. 5 and 6. The results from the Bayesian models were approximately identical to the maximum-likelihood models and are omitted. On the basis of the similarity of results, the main text used the more familiar frequentist results including the monthly adjustment.

Supplementary Table 1 numerically summarizes the results of the statistical analysis used in the main text where the 800 cm^{-1} brightness temperature threshold is 3 K.

Controlling for N_2O. The methods used to determine CH_4 surface radiative forcing can be biased by N_2O. Figure 2b shows this due to the substantial amount of overlap in spectral radiance changes from perturbations from N_2O and CH_4. However, the vertical profiles of N_2O collected by the ARM-Airborne Carbon Measurements (ACME) missions[35] at the SGP show that N_2O mixing ratios at altitude are highly vertically correlated with the surface (see the insets of Fig. 2c) and vary by less than 1 ppbv seasonally.

Moreover, these differ very little from measurements at the MLO. The error incurred in CH_4 forcing from utilizing monthly averaged MLO N_2O observations instead of in situ ARM-ACME N_2O observations was maximized at 1.2% of the CH_4 forcing.

N_2O can still bias CH_4 forcing because it is emitted after precipitation following the nearby fresh application of nitrogen-based fertilizer[68], causing > 5 ppbv deviations from the background N_2O mixing ratio. Next-Generation Radar (NEXRAD) data[69] were used to screen data to remove those observations for which precipitation had occurred in the previous 24 h.

Instantaneous error. There are several sources of error in the determination of the surface forcing from the AERI measurements. They include: spectroscopic error in LBLRTM; AERI measurement error; error in the temperature, water vapour, CO_2 or O_3 inputs to LBLRTM inputs; and a contribution of unknown aerosol or cloud condensates to the AERI observations. While the error contributions from the first of these are outside of the scope of this analysis, we can perform a top-down estimate of errors from the last three with AERI measurements and LBLRTM calculations using inputs from simultaneous aircraft profiles.

Surface radiative forcing time series from the aircraft data were derived from differencing AERI observations with counterfactual calculations. These were compared with the surface radiative forcing time series computed by differencing an LBLRTM calculation with the aircraft-observed profile of CH_4 and N_2O and the counterfactual calculation.

Supplementary Fig. 8 shows the standard deviation of AERI-observed and aircraft-derived surface radiative forcing. Figure 3 shows that an abscissa value of 3 K corresponds to an ordinate value of 0.14 W m^{-2}, which is thus our estimate of the 1σ instantaneous error in radiative forcing.

Ethane data analysis. Supplementary Fig. 9a,b shows time-series analyses of ethane (C_2H_6) flask data. Non-methane hydrocarbon flask data from SGP were first filtered for outliers; values that deviated more than 2σ from a running median were excluded from trend analyses. Filtered data were then uploaded to the National Oceanic and Atmospheric Administration (NOAA) server for filtering and trends were determined using a previously published method[70].

Clear-sky bias. We evaluate the potential for clear-sky bias in the determination of CH_4 surface radiative forcing. We estimate this bias by recalculating the Broadband Heating Rate Profiles[71] at the SGP for 2010 based on pre-industrial CH_4 mixing ratios and comparing those to the original Broadband Heating Rate Profiles, containing time-varying CH_4 derived from the nearest grid box from CarbonTracker-CH4[72]. We then subset the data identified as clear-sky in the Radiatively Important Parameters Best Estimate product[73].

We find that most of the forcing is in the clear-sky but that the all-sky surface forcing is 0.065 W m^{-2}, or 33%, less than the clear-sky forcing. This finding is expected because of non-negligible overlap between broadband cloud absorption and CH_4 absorption, thereby masking CH_4 forcing. This cloud-masking may vary year-to-year. Currently, the independent estimates of cloud vertical profiles produce residual spectra with signatures of clouds, so the effect of CH_4 cannot be isolated under all-sky conditions.

Non-methane contributions to observed signal. The possibility that condensates or non-methane gaseous atmospheric constituents are contributing to the observed CH_4 surface forcing must be considered. The contribution of condensates can be excluded because they produce broadband signals that are not observed in the residual spectra. We can also address the non-methane gaseous constituent question by determining the effects of perturbations in the atmospheric concentrations of 32 additional species with spectroscopy tabulated in HITRAN[21], and found their contributions to be at least five orders of magnitude smaller than for CH_4.

Flask-based observations. At the SGP site, samples were collected into a pair of 2.5 l glass flasks on a weekly basis from the top of the central facility 60 m tower. Flask collection started in April 2002 and is currently ongoing. The collection of a pair of samples allows basic quality assessment and control. These observations are part of the NOAA's Global Greenhouse Gases Reference Network[74]. Flasks are collected in the afternoon, when the planetary boundary layer is well developed and observations are representative of a large area. Aircraft profiles of CH_4 and N_2O were recorded on approximately a bi-monthly basis from 2002 until the present (see Supplementary Fig. 7a,b).

Ground-based and aircraft-based flasks are analysed after they are collected at NOAA/Earth System Research Laboratory by gas chromatography, and measurements are reported against World Meteorological Organization CH_4-X2004 and N_2O-X2006A scales. Flask-based observations are shown to have uncertainties of less than 1.2 ppbv for CH_4 and 0.4 ppbv for N_2O.

Aircraft validation. Aircraft profiles of CH_4 and N_2O above the SGP site were recorded on approximately a weekly basis with flask observations from 2002 until the present. Before 2006, the flasks were collected only at 0.6 and 3.6 km, but since then, flasks were collected at 12 elevations between 0.5 km and 5.5 km above sea level (see Supplementary Fig. 7a,b).

Single-site analysis. The analysis presented here focused on the SGP site. Several other ARM sites exist, including the North Slope of Alaska (NSA) site, and AERI data from that site were analysed for previous work[27]. For the CH_4 analysis, however, differences in the instrumental noise in the AERI instrument at NSA greatly complicated the analysis there. In particular, the Extended-Range AERI at NSA has an expanded spectral range compared to the AERI at the SGP, leading to higher instrumental (random) noise over 1,200–1,350 cm^{-1} spanning the dominant CH_4 absorption feature[75].

Residual brightness temperature threshold rationale. The rationale for choosing a threshold of 3 K brightness temperature is based on balancing the number of data points with error in the CH_4 surface forcing determination, both of which will increase with increasing threshold values. Another related factor for the determination of an appropriate threshold is the importance of observations throughout the year. The 3 K threshold enables a determination of the seasonal cycle in surface forcing at the SGP site and summertime multi-year trends at the NSA site. Supplementary Fig. 3 shows the relationships between the 800 cm^{-1} brightness temperature residual threshold and the number of data points.

Code availability. The computer code developed for this research was written in Matlab and will be made available upon request.

Data availability. The ARM data and radiative transfer codes used in this analysis are freely available to download from http://www.archive.arm.gov/discovery/ and http://rtweb.aer.com, respectively. The following are URLs from which input data can be downloaded:

MERRA: https://disc.sci.gsfc.nasa.gov/datasets?page=1&keywords=merra

CarbonTracker-CO2: ftp://aftp.cmdl.noaa.gov/products/carbontracker/co2/molefractions/ CarbonTracker-CH4: ftp://aftp.cmdl.noaa.gov/products/carbontracker/ch4/molefractions/

NOAA CH_4 data: http://ds.data.jma.go.jp/gmd/wdcgg/pub/data/current/ch4/

NOAA N_2O data: ftp://aftp.cmdl.noaa.gov/data/hats/n2o/insituGCs/CATS/daily/mlo_N2O_Day.dat

NOAA C_2H_6 data: http://ds.data.jma.go.jp/gmd/wdcgg/pub/data/current/vocs/ethane/event/

References

45. Atmospheric Emitted Radiance Interferometer (AERICH1). *2000-01-01 to 2015-06-01, 36.605 N 97.485 W: Southern Great Plains (SGP) Central Facility, Lamont, OK, Atmospheric Radiation Measurement (ARM) Climate Research Facility Data Archive* (ARM Data Discovery, accessed 1 June 2016); https://doi.org/10.5439/1025143
46. *ARM Best Estimate Data Products (ARMBEATM). 2002-01-01 to 2012-12-31, 36.605 N 97.485 W: Southern Great Plains (SGP) Central Facility, Lamont, OK (C1). Compiled by X. Chen and S. Xie. Atmospheric Radiation Measurement (ARM) Climate Research Facility Data Archive* (ARM Data Discovery, accessed 1 June 2015); https://doi.org/10.5439/1039931
47. Rienecker, M. M. et al. MERRA: NASA's modern-era retrospective analysis for research and applications. *J. Clim.* **24**, 3624–3648 (2011).
48. Peters, W. et al. An atmospheric perspective on North American carbon dioxide exchange: CarbonTracker. *Proc. Natl Acad. Sci. USA* **104**, 18925–18930 (2007).
49. Hall, B. D., Dutton, G. S. & Elkins, J. W. The NOAA nitrous oxide standard scale for atmospheric observations. *J. Geophys. Res. Atmos.* **112**, D09305 (2007).
50. Clough, S. A. et al. Atmospheric radiative transfer modeling: a summary of the AER codes. *J. Quant. Spectrosc. Rad. Trans.* **91**, 233–244 (2005).
51. Rothman, L. S. et al. The HITRAN 2008 molecular spectroscopic database. *J. Quant. Spectrosc. Rad. Trans.* **110**, 533–572 (2009).
52. Alvarado, M. J. et al. Impacts of updated spectroscopy on thermal infrared retrievals of methane evaluated with HIPPO data. *Atmos. Meas. Tech.* **8**, 965–985 (2015).
53. Li, J. Gaussian quadrature and its application to infrared radiation. *J. Atmos. Sci.* **57**, 753–765 (2000).
54. Turner, D. D., Knuteson, R. O., Revercomb, H. E., Lo, C. & Dedecker, R. G. Noise reduction of Atmospheric Emitted Radiance Interferometer (AERI) observations using principal component analysis. *J. Atmos. Ocean. Technol.* **23**, 1223–1238 (2006).
55. Wang, J. et al. Corrections of humidity measurement errors from the Vaisala RS80 Radiosonde – application to TOGA COARE data. *J. Atmos. Ocean. Technol.* **19**, 981–1002 (2002).
56. Turner, D. D. et al. Dry bias and variability in Vaisala radiosondes: The ARM experience. *J. Atmos. Ocean. Technol.* **20**, 117–132 (2003).
57. Weatherhead, E. C. et al. Factors affecting the detection of trends: Statistical considerations and applications to environmental data. *J. Geophys. Res.* **103**, 17149–17161 (1998).
58. Liu, X., et al. OMI ozone profile and tropospheric ozone and cross evaluations with chemical transport models, *AGU Meeting of the Americas*, A31A-22 (2013).
59. Kuhn, M. & Johnson, K. *Regression Trees and Rule-Based Models in Applied Predictive Modeling* (Springer, New York, 2013).
60. Shumway, R. H. & Stoffer, D. S. *Time Series Analysis and Its Applications* (Springer, New York, 2000).
61. Ivosev, G., Burton, L. & Bonner, R. Dimensionality reduction and visualization in principal component analysis. *Anal. Chem.* **80**, 4933 (2008).
62. Frank, R. J., Davey, N. & Hunt, S. P. Time series prediction and neural networks. *J. Intell. Robot. Syst.* **31**, 91–103 (2001).
63. Casella, G. & Berger, R. L. (eds) in *Statistical Inference* Ch. 7.2.2 (Duxbury Press, Ithaca, 2002).
64. Ravishanker, N. & Dey, D. *A First Course in Linear Model Theory* (Chapman and Hall/CRC, Boca Raton, 2002).
65. Casella, G. & Berger, R. L. (eds) in *Statistical Inference* Ch. 10.4 (Duxbury Press, Ithaca, 2002).
66. Gilks, W. R., Richardson, S. & Spiegelhalter, D. J. *Markov Chain Monte Carlo in Practice* (Chapman and Hall/CRC, Boca Raton, 1995).
67. Kass, R. E. & Raftery, A. E. Bayes factors. *J. Am. Stat. Assoc.* **90**, 773–795 (1995).
68. Bouwman, A. F., Boumans, L. J. M. & Batjes, N. H. Modeling global annual N_2O and NO emissions from fertilized fields. *Glob. Biogeochem. Cycles* **16**, 1080 (2002).
69. Fulton, R. A., Breidenbach, J. P., Seo, D. J., Miller, D. A. & O'Bannon, T. The WSR-88D rainfall algorithm. *Weather Forecast.* **13**, 377–395 (1998).
70. Thoning, K. W., Tans, P. P. & Komhyr, W. D. Atmospheric carbon-dioxide at Mauna Loa observatory. 2. Analysis of the NOAA GMCC data, 1974–1985. *J. Geophys. Res.* **94**, 8459–8565 (1989).
71. McFarlane, S. A. *ARM's Progress on Improving Atmospheric Broadband Radiative Fluxes and Heating Rates* (AMS, 2016); https://doi.org/10.1175/AMSMONOGRAPHS-D-15-0046.1
72. Bruhwiler, L. M. et al. CarbonTracker-CH4: an assimilation system for estimating emissions of atmospheric methane. *Atmos. Chem. Phys.* **14**, 8269–8293 (2014).
73. McFarlane, S., Shippert, T. and Mather, J. *Radiatively Important Parameters Best Estimate (RIPBE): An ARM Value-Added Product* DOE Technical Report SC-ARM/TR-097 (US Department of Energy, 2011).
74. Dlugokencky, E. J., Steele, L. P., Lang, P. M. & Masarie, K. A. The growth rate and distribution of atmospheric methane. *J. Geophys. Res.* **99**, 17021–17043 (1994).
75. Knuteson, R. O. et al. Atmospheric emitted radiance interferometer. Part II: Instrument performance. *J. Atmos. Ocean. Technol.* **21**, 1777–1789 (2004).